Batteries & Supercaps

Articles
doi.org/10.1002/batt.202000152

Chemistry
Europe
European Chemical
Societies Publishing

Encapsulating Oxygen-Deficient TiNb$_{24}$O$_{62}$ Microspheres by N-Doped Carbon Nanolayer Boosts Capacity and Stability of Lithium-Ion Battery

Jiangmin Jiang,[a, b] Zhiwei Li,[a] Guangdi Nie,[c] Ping Nie,[d] Zhenghui Pan,[b] Zongkui Kou,[b] Qiang Chen,[b, e] Qi Zhu,[a] Hui Dou,[a] Xiaogang Zhang,*[a] and John Wang*[b]

Most of the insertion anode materials are approaching their specific capacity limitations. TiNb$_{24}$O$_{62}$, combining the merits of high theoretical capacity, large working potential and excellent safety, is a promising candidate for lithium-ion batteries (LIBs). However, its poor intrinsic conductivity and relatively sluggish reaction kinetics hinder its wide applications. Herein, we encapsulate the oxygen-deficient TiNb$_{24}$O$_{62}$ microspheres by highly conductive N-doped carbon nanolayer (DTNO@NC), where TiNb$_{24}$O$_{62}$ is purposely made to exhibit oxygen deficiency, by aerosol spray followed by co-carbonization of the electronically coupled polydopamine (PDA) coating layer. The

oxygen-deficient engineering for TiNb$_{24}$O$_{62}$ improves the intrinsic conductivity and active sites, while the PDA derived N-doped carbon coating layer not only stabilizes the interface between the electrode and electrolyte, but also further enhances the overall conductivity. As a result, the as-fabricated DTNO@NC electrode delivers excellent Li$^+$ ion storage capacity (270 mAh g^{-1} at 0.1 A g^{-1}) and superior cycling lifespan (capacity retention of 90% after 1000 cycles). This work demonstrates the effectiveness of integrating an oxygen-deficient structure of intercalation-type anode material with a carbon encapsulating nanolayer in enabling the overall energy storage performance.

1. Introduction

Lithium-ion batteries (LIBs) have been dominating the power sources for portable and wearable electronics market over the past two decades, and are now quickly expanding to electric and hybrid electric vehicles. The key performance parameters of advanced battery systems include a large energy density, high power density, good cyclic lifespan, and safety.[1–4] Because

[a] Dr. J. Jiang, Dr. Z. Li, Q. Zhu, Prof. H. Dou, Prof. X. Zhang
Jiangsu Key Laboratory of Electrochemical Energy Storage Technology,
College of Material Science and Engineering,
Nanjing University of Aeronautics and Astronautics,
Nanjing, 210016, China
E-mail: azhangxg@nuaa.edu.cn

[b] Dr. J. Jiang, Dr. Z. Pan, Dr. Z. Kou, Dr. Q. Chen, Prof. J. Wang
Department of Materials Science and Engineering,
National University of Singapore,
117574, Singapore
E-mail: msewangj@nus.edu.sg

[c] Prof. G. Nie
Industrial Research Institute of Nonwovens & Technical Textiles,
College of Textiles and Clothing,
Qingdao University,
Qingdao, 266071, China

[d] Dr. P. Nie
Key Laboratory of Preparation and Application of Environmental Friendly Materials,
College of Chemistry,
Jilin Normal University,
Siping, 136000, China

[e] Dr. Q. Chen
State Key Laboratory of Advanced Technology for Materials Synthesis and Processing,
Wuhan University of Technology,
Wuhan, 430070, China

of the relatively large specific capacity (372 mAh g^{-1}) and long cycle stability, graphite anode has been widely used in LIBs. However, the low working potential (~0.1 V vs. Li/Li$^+$), the likely formation of Li dendrite, and safety issues in connection with the use of organic electrolyte are among the major concerns. Besides, its poor Li$^+$ diffusion kinetics and the formation of thick solid electrolyte interphase (SEI) often lead to inferior rate capability.[5] In this regard, "zero-strain" Li$_4$Ti$_5$O$_{12}$ has been investigated as an alternative candidate, which presents a relatively fast ion diffusion rate and high working potential (~ 1.57 V), thus could avoid the irreversible SEI formation and minimize the likelihood of Li dendrite growth, together with high safety and outstanding cycle stability.[6] Nevertheless, it has an inherent theoretical specific capacity of only 175 mAh g^{-1}, which cannot meet the demand for high energy density. Although alternative anode materials, such as metal oxides,[7–9] sulfides,[10–12] and silicon-based materials have been exploited,[13–15] most of them inevitably undergo a large volume expansion and unsatisfactory cycling stability.

The insertion-type TiNb$_2$O$_7$ anode was first proposed by Goodenough's group in 2011,[16] and since then a series of titanium (Ti)-niobium (Nb) oxides (such as TiNb$_2$O$_7$,[17–22] TiNb$_6$O$_{17}$,[23–26] Ti$_2$Nb$_{10}$O$_{29}$,[27–31] and Ti$_2$Nb$_{14}$O$_{39}$,[32] etc.) have been considered as promising anode materials for LIBs. They exhibit multiple redox couples of Nb^{5+}/Nb^{4+}, Nb^{4+}/Nb^{3+} and Ti^{4+}/Ti^{3+}, and can give rise to excellent theoretical capacities, together with high safety features on account of a comparatively high Li$^+$ storage potential (~1.7 V). As a relatively new type of Ti–Nb oxides, TiNb$_{24}$O$_{62}$ has been prepared by a solvothermal method, and explored as the anode for LIBs in 2016.[33] It is of a typical Wadsley-Roth phase, which derives from the ReO$_3$ crystal structure, along with the disordered MO$_6$ (M=Ti or Nb)

octahedral to accommodate additional Li$^+$ ions.[34,35] TiNb$_{24}$O$_{62}$ as an anode is expected to show the largest theoretical capacity of ~402 mAh g^{-1} among all Ti–Nb oxides. Unfortunately, its poor intrinsic conductivity (electronic and ionic) and relatively sluggish reaction kinetics in bulk forms are apparently the down-side issues.

To improve the electrochemical performance of the anode material, for instance, Lee et al. developed a holey graphene-wrapped structure via a solvothermal approach to enhance the electronic conductivity.[36] Shu et al. then reported the electro-spinning and carbon coating combined strategy to optimize the electrochemical performance.[37] Alternatively, the introduction of certain defects (e.g. oxygen vacancies) in the material itself is another effective strategy to improve the conductivity and the overall electrochemical properties.[38–41] Oxygen deficiencies are known to facilitate ion and charge transfers being able to significantly raise the conductivity, decrease the energy barriers, and thus increase Li$^+$ diffusion coefficients.[42–45] To date, metal thermal reduction, electrochemical reduction, and high-temperature hydrogenation have been reported to induce oxygen deficiencies in oxide-based anodes.[46–49] However, the choice of a technique for oxygen deficiencies has to be considered with other parameters, such as the cost and production efficiency for an industrial process.
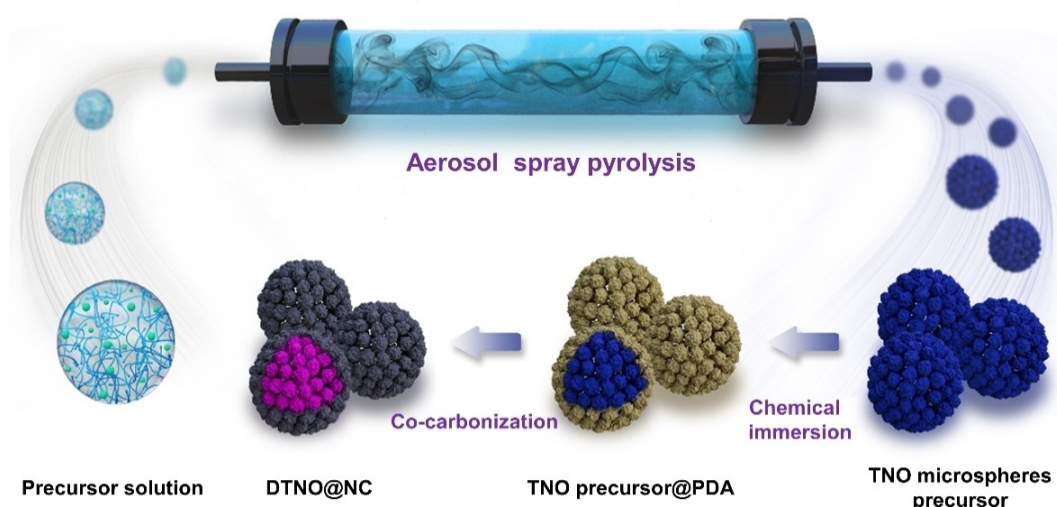
Herein, we propose a facile and cost-effective aerosol spray and chemical immersion strategy to prepare the TiNb$_{24}$O$_{62}$-polydopamine precursor, where the N-doped carbon encapsulation of TiNb$_{24}$O$_{62}$ microspheres is completed together with the formation of oxygen-deficiency defects (DTNO@NC), conducted in an argon atmosphere. The introduction of oxygen deficiencies in TiNb$_{24}$O$_{62}$ increases its intrinsic conductivity, the population of reaction sites and pseudocapacitance, while the carbon coating layer improves the overall conductivity and structural stability. Benefiting from the synergistic effect of the intrinsic oxygen-deficient structure and the extrinsic carbon coating nanolayer, the as-fabricated DTNO@NC electrode exhibits superior electrochemical performance compared to the pristine TiNb$_{24}$O$_{62}$ (TNO) electrode, including a high specific capacity of 270 mAh g^{-1} at 0.1 A g^{-1}, excellent rate ability (172 mAh g^{-1} at 5 A g^{-1}), and outstanding cycling stability for 1000 cycles (capacity retention of 90%).
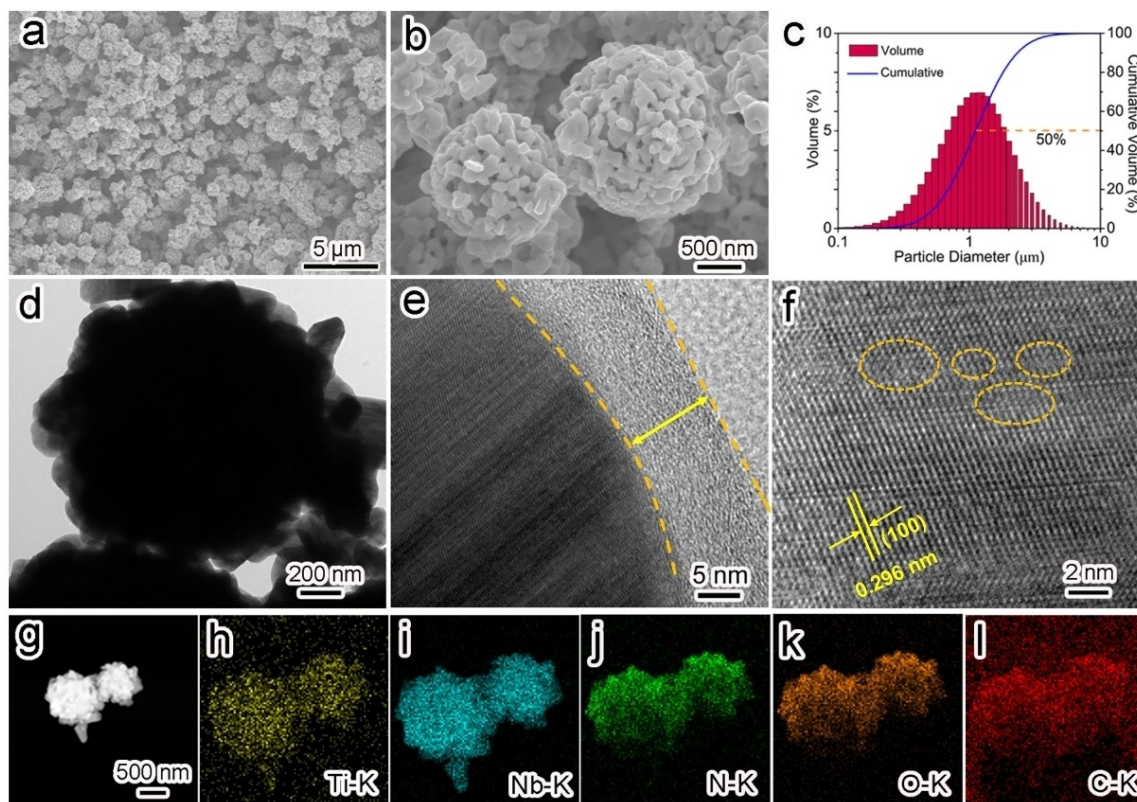
2. Results and Discussion

The synthesis processes of the TNO and DTNO@NC samples are shown in Figure 1. Firstly, the titanium and niobium sources were uniformly dispersed in a mixed solvent of ethanol and acetic acid. The precursor of TNO microspheres was obtained through aerosol spray pyrolysis. It should be noted here that the aerosol spray pyrolysis is a facile, cost-effective, and continuous process, which enables the preparation of nano-structured materials with desired morphologies and composited structures.[50–52] Afterward, the TNO microsphere precursors were chemically immersed in an alkaline polydopamine (PDA) solution to obtain the TNO@PDA, and they were then co-carbonized to prepare the oxygen-deficient and N-doped TNO (DTNO@NC) in an argon atmosphere. Notably, this structural design for defect engineering and carbon coating neither requires any additional structural templates, hydrogen atmosphere or metals, nor generates chemical contaminants, and thus is considered as a cost-effective synthesis strategy to improve conductivity and structural stability. For comparison, the pristine TNO microspheres were acquired from the high-temperature calcination of TNO precursors under the air atmosphere.

The morphologies of the as-prepared samples were studied using scanning electron microscopy (SEM) and transmission electron microscopy (TEM). As shown in Figure 2a and 2b, the DTNO@NC exhibits a rather uniform monodispersed micro-sphere structure, which was formed by the nanoparticle self-assembly via aerosol spray pyrolysis process. The TNO precursor

Figure 1. Schematic illustration of the synthesis process of the TNO and DTNO@NC.
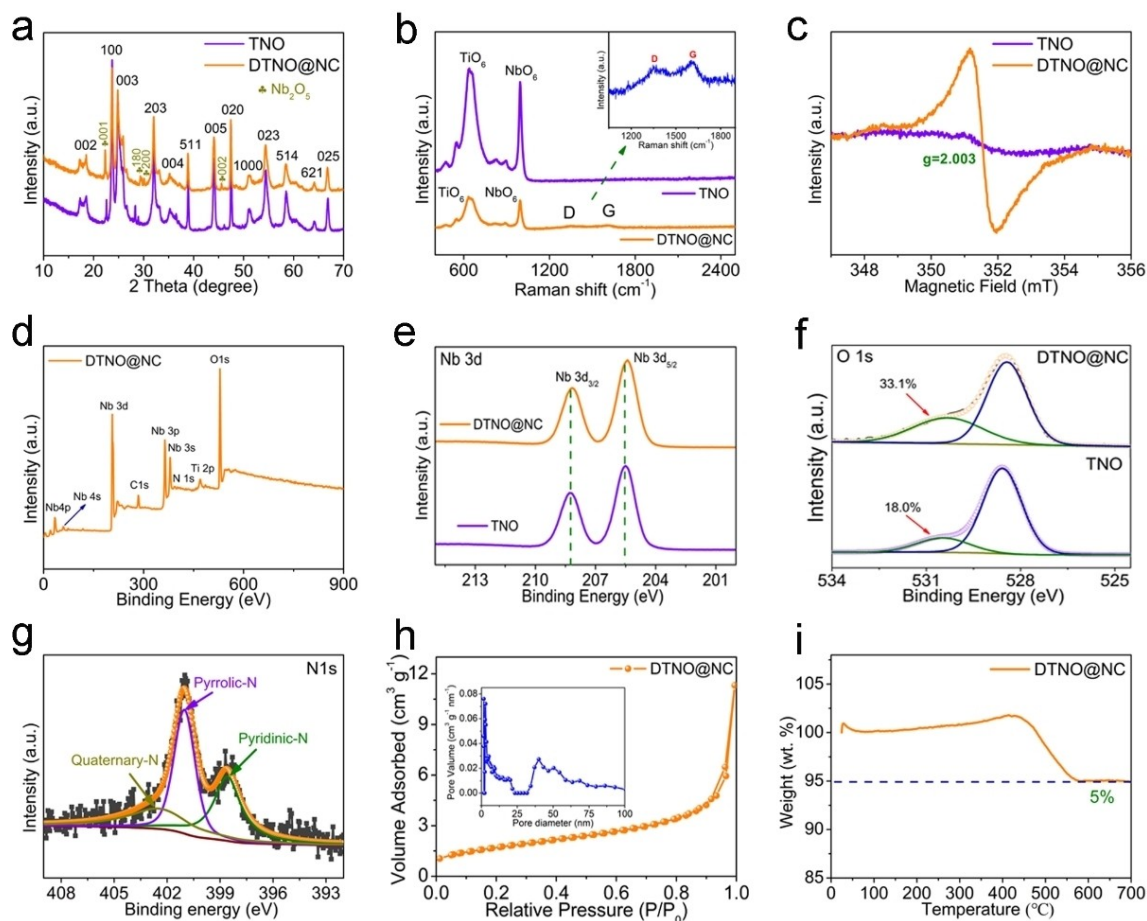
Figure 2. a, b) SEM images of the DTNO@NC at different magnifications. c) Particle size distribution curve, and d–f) TEM and HRTEM images of the DTNO@NC. g) STEM of the DTNO@NC, and the corresponding elemental mapping of h) Ti, i) Nb, j) N, k) O, and l) C, respectively.

and TNO samples show similar monodispersed microsphere structure (Figure S1 and S2), implying they have good thermal stability during the high-temperature treatment process. According to the analysis studies of the particle size distribution (Figure 2c), the DTNO@NC displays an average diameter of about ~960 nm. In particular, the commonly used parameter of D50 shows that the particle diameter comprising 50% of the total sample volume is about ~1.1 μm. The TEM micrograph shown in Figure 2d reveals that the outer surface of the DTNO@NC microspheres was coated with a uniform carbon nanolayer with a thickness of about ~10 nm (Figure 2e). As shown in Figure S3, the selected area electron diffraction (SAED) pattern of the DTNO@NC displays sharp diffraction spots and bright stripes, suggesting the single-crystal feature and good crystallinity of the nanoparticle subunits.[53] Besides, a clear lattice fringe with a distance of 0.296 nm is observed in Figure 2f, which is corresponding to the (100) plane of the TNO. It can be found that DTNO@NC exhibits an obvious degree of oxygen-deficient defects in the crystal structure (marked by yellow circles), which were apparently caused by oxygen deficiencies. Moreover, the elemental mapping images show that all elements (such as Ti, Nb, O, C, N) are uniformly distributed on the surface of the DTNO@NC (Figure 2g–l), revealing that the oxygen-deficient TNO microspheres have been successfully encapsulated within the N-doped carbon nanolayer.

The crystal structures of the TNO and DTNO@NC were investigated by X-ray diffraction (XRD). As shown in Figure 3a, all the main diffraction peaks can be indexed to a Wadsley-Roth shear structure with the C_2 space group.[36] Whereas there have some low-intensity diffraction peaks cannot be indexed to the pure TNO, which is corresponding to a small amount of the Nb_2O_5 phase (PDF#27-1003). Because of the high contents and proportions of the Nb element in TNO, it is easy to form a small amount of Nb_2O_5 phase in an air atmosphere.[33] Notably, the peaks ascribed to the N-doped carbon are overlapped with the (100) and (005) diffraction peaks of the TNO. Raman spectra show two peaks that correspond to the unique bands of TiO_6 and NbO_6 (Figure 3b), and this further confirms that the TNO is well established.[37] Besides, the additional two peaks are located at around 1350 and 1600 cm^{-1} of the DTNO@NC (inset of Figure 3b), which are ascribed to the D-band and G-band of the carbon material, indicating that the N-doped carbon nanolayer has been successfully coated on the surface of the oxygen-deficient TNO microspheres. The encapsulation of the N-doped carbon nanolayer is an effective strategy to improve the electronic conductivity; it can not only accelerate the electrochemical reaction kinetics but also endow of electrode materials with excellent stability in the long-term cycles with a non-aqueous electrolyte.

Electron paramagnetic resonance (EPR) was employed to directly confirm the existence of oxygen deficiencies. As shown in Figure 3c, the TNO shows almost no characteristic EPR

Batteries & Supercaps

Articles
doi.org/10.1002/batt.202000152

Chemistry Europe
European Chemical
Societies Publishing

Figure 3. a) XRD patterns, b) Raman spectra, and c) EPR spectra of the TNO and DTNO@NC. d) The survey, e) Nb 3d, and f) O 1s XPS spectra of the TNO and DTNO@NC. g) High-resolution N1s spectra of the DTNO@NC. h) Nitrogen adsorption-desorption isotherms (insertion image: pore size distribution) and i) TG curves of the DTNO@NC.

response signal, illustrating that no oxygen deficiencies were formed. As a comparison, the DTNO@NC exhibits a significant EPR response signal at around $g = 2.003$, which directly demonstrate the existence of oxygen deficiencies. Note that the electronically coupled PDA polymers play a crucial role in introducing oxygen deficiencies, which were produced from the direct oxidation of dopamine monomers with extending π-conjugated electron systems, bringing oxygen deficiencies into the crystal structure of the TNO, and accompanied with the injection of electrons into its conduction band, possessing high conductivity.[38,54,55] Besides, the high-temperature carbothermal reduction can also generate oxygen deficiencies in the argon atmosphere. Moreover, N-doped carbon is known to processes various defects, for example, the existence of unpaired electrons in pyridinic-N and pyrrolic-N, respectively.

To further confirm the formation of oxygen deficiencies, the chemical nature and the valence states in each sample were investigated by X-ray photoelectron spectroscopy (XPS). The titanium (Ti), niobium (Nb) and oxygen (O) element peaks can be observed in the survey XPS spectra of TNO and DTNO@NC (Figure 3d and S4a). The additional carbon (C) and nitrogen (N) peaks are detected in the survey XPS spectrum of DTNO@NC, supporting the presence of the N-doped carbon-coating layer.

As shown in Figure 3e, there are two peaks at 208.3 and 205.5 eV for TNO, which are ascribed to Nb $3d_{3/2}$ and Nb $3d_{5/2}$, respectively. It can be seen that they have moved to the lower binding energy of 208.1 and 205.3 eV for DTNO@NC, again demonstrating the successful introduction of oxygen deficiencies.[56] The migration of the Ti 2p peaks is relatively insignificant (Figure S4b), because the titanium content is rather low in the NTO structure. As shown in Figure 3f, the high-resolution O 1s spectra of the NTO and DTNO@NC can be divided into two peaks, which are located at 528.6 and 530.5 eV, corresponding to the lattice oxygen with full complement and oxygen ions in oxygen-deficient regions, respectively.[57] The percentage of the oxygen-deficient peak area in DTNO@NC (33.1%) is increased compared to that of TNO (18.0%), this result further supports the existence of oxygen deficiencies in DTNO@NC.
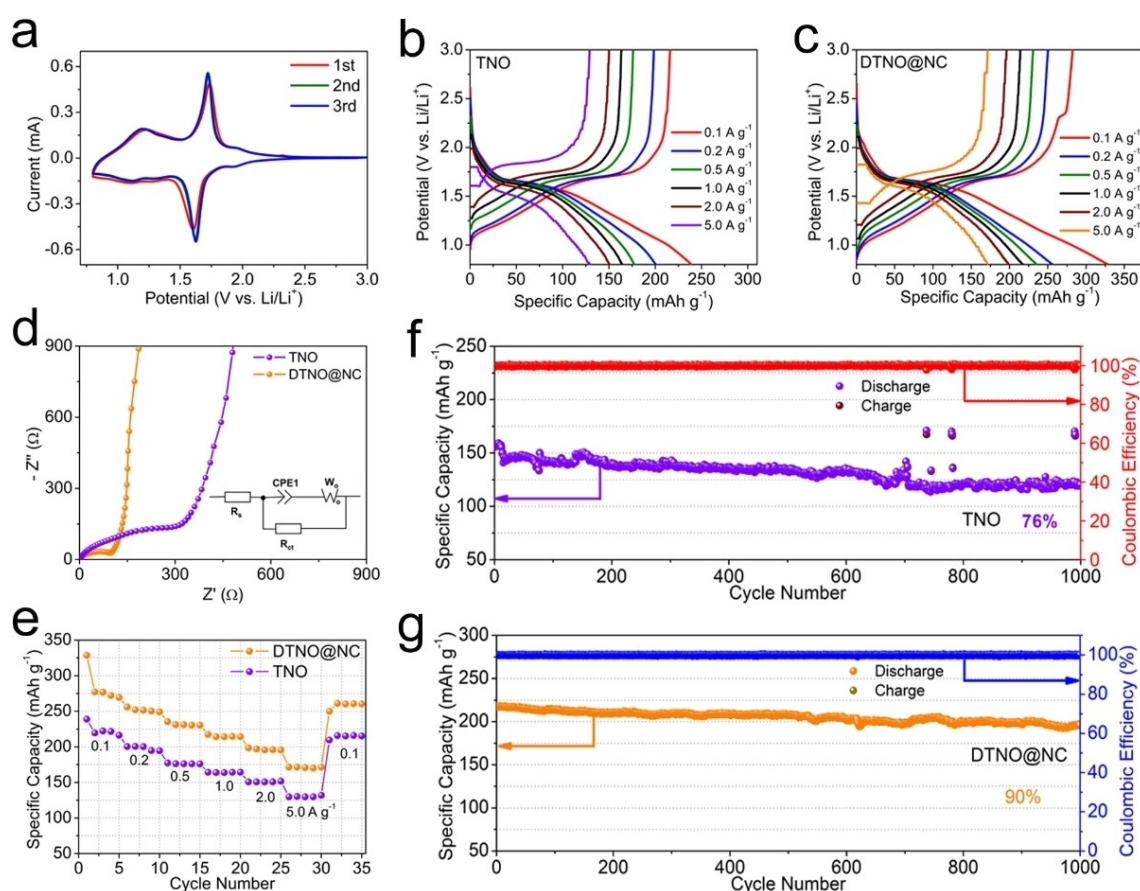
The high-resolution N 1s spectrum can be divided into three peaks (Figure 3g), which are located at 398.6, 401.0, and 402.4 eV, corresponding to the pyridinic-N, pyrrolic-N, and quaternary-N, respectively.[58,59] The N-doped carbon can not only improve the electronic conductivity of the composite anode but also enhance the interface wettability between the electrode and electrolyte. Besides, the specific surface areas

(SSAs) and pore size distributions of the samples were measured by the N_2 adsorption-desorption isotherms (Figure 3h and S5). In particular, the TNO and DTNO@NC have relatively small SSAs with 4.6 and 6.1 $cm^2 g^{-1}$, respectively. The DTNO@NC displays a H3 hysteresis loop in a relative pressure range of 0.8~1.0 (insert of Figure 3h), indicating the existence of mesopores, which would be beneficial to the Li^+ rapid transmission and electrolyte infiltration.[60] Moreover, thermogravimetric analysis (TGA) was performed to detect the carbon weight ratio. As shown in Figure 3i, the carbon content in the DTNO@NC was calculated to be about 5%.

The lithium-storage behavior of the TNO and DTNO@NC were investigated by cyclic voltammetry (CV) in half-cells within the working voltage range of 0.8~3.0 V. It can be seen that both the TNO and DTNO@NC possess similar CV patterns, and the first cycle curve is slightly different from those in the subsequent cycles at the scan rate of 0.2 $mV s^{-1}$ (Figure 4a and S6). Such a difference can well be derived from the electronic structure change of the TNO, since Li^+ is not completely reversible in the first insertion and extraction process. This irreversible phenomenon has been observed in other Ti–Nb oxides, such as $TiNb_2O_7$ and $Ti_2Nb_{10}O_{29}$.[61,62] There are three pairs of redox peaks in the TNO and DTNO@NC can be seen in the second cycle. In particular, one pair of cathodic/anodic peaks are at around ~1.9 V, corresponding to the $Ti^{4+/3+}$ redox

couple. Another pair of strong redox located at about 1.62/ 1.73 V is attributed to the $Nb^{5+/4+}$ redox couple. The third pair of peaks is observed at 0.8~1.4 V, attributed to the $Nb^{4+/3+}$ valence variation.[63] Notably, these intercalation potentials are much higher than the nucleation potential of metallic lithium dendrites, suggesting that the TNO materials can be employed as a highly safe anode in suppressing the dendrite growth. The CV curves of the TNO and DTNO@NC are almost completely overlapped after the first cycle, implying the excellent reversibility.

To further evaluate their electrochemical performance, the galvanostatic charge-discharge (GCD) tests were conducted and shown in Figure 4b and 4c. During the discharge process, the TNO and DTNO@NC show a sloping line down to around ~1.7 V, corresponding to the solid-solution process. Afterwards, they have an obvious plateau at about 1.6~1.7 V, attributed to the two-phase transformation process. Besides, a further sloping line until ~0.8 V belongs to another solid-solution process, which is consistent with the results of the CV curves (Figure 4a).[64] The DTNO@NC exhibits a higher reversible specific capacity, compared with TNO whether at low (0.1 $A g^{-1}$) or high current density (5.0 $A g^{-1}$), suggesting that the exposed oxygen deficiencies provide more electrochemical reaction active sites. At the high current density of 5 $A g^{-1}$, the TNO is significantly more polarized than DTNO@NC, indicating that the

Figure 4. a) CV curves of the DTNO@NC at 0.2 $mV s^{-1}$. GCD profiles of the b) TNO and c) DTNO@NC at different densities. d) Nyquist plots and equivalent circuit (inset), and e) rate capabilities of the TNO and DTNO@NC. Long-term cycling stability of the f) TNO and g) DTNO@NC at a current density of 1 $A g^{-1}$.

encapsulating of N-doped carbon nanolayer has effectively improved the overall electronic conductivity.

Electrochemical impedance spectroscopy (EIS) was performed to further study the charge transfers kinetics of the samples. As shown in Figure 4d, both the TNO and DTNO@NC possess a depressed semicircle in the high-frequency area and an almost vertical line in the low-frequency area, which represents the charge transfer impedance and Li$^+$ solid-state diffusion resistance, respectively.[65] In brief, the DTNO@NC (102.4 Ω) exhibits a smaller charge transfer resistance (R_{ct}) compared with the TNO (376.1 Ω) by the equivalent circuit fitting (inset of Figure 4d), suggesting that the oxygen-deficiency engineering and N-doped carbon encapsulation strategy are able to reduce the reaction resistance (Table S1), which is in agreement with the low polarization of the DTNO@NC at high current density (Figure 4c).

Additionally, DTNO@NC delivers a superior rate capability compared to the TNO electrode especially at the high current density (Figure 4e). The reversible specific capacities of the DTNO@NC are 270, 249, 230, 214, 196, 172, and 260 mAh g^{-1} at current rates of 0.1, 0.2, 0.5, 1.0, 2.0, 5.0 and 0.1 A g^{-1}, respectively. In contrast, the bare TNO displays an obvious capacity drop at high current density, which delivers specific capacities of 222, 195, 176, 164, 152, 130 and 215 mAh g^{-1} at the corresponding current densities. Moreover, the DTNO@NC electrode shows a superior cycle stability compared with that of the TNO electrode. As shown in Figure 4f and 4g, the DTNO@NC electrode possesses a high reversible capacity of 197 mAh g^{-1} with the excellent capacity retention of 90% at a current density of 1 A g^{-1} after 1000 cycles, while the reversible capacity for the TNO electrode is 121 mAh g^{-1} with a capacity retention of 76% after the same cycling. Furthermore, the DTNO@NC electrode exhibits the lower R_f and R_{ct} impedances after 1000 charge-discharge cycles by the equivalent circuit fitting (Figure S7a and 7b), suggesting that smaller charge impedances and transfer barriers in the DTNO@NC electrode (Table S1), leading to the much improved cycle performance.

To further illustrate the advantages of the two-pronged strategy by oxygen-deficient engineering and N-doped carbon coating layer in the DTNO@NC, the TNO precursor was calcined at high-temperature in an argon atmosphere to obtain the defective TNO (DTNO) microspheres, where the defect characteristics and electrochemical performance were then investigated. Specifically, the DTNO shows an EPR response signal at around g = 2.003 (Figure S8), indicating the oxygen deficiency in DTNO microspheres that had been generated by the high-temperature treatment in an argon atmosphere. As such, the rate capability of the DTNO electrode is better than that of the TNO. It was however not comparable with the DTNO@NC anode, which exhibits better rate performance especially at the high current density, e.g., 5 g^{-1} (Figure S9). The capacity retention of the DTNO electrode is 81% of the initial value at the current density of 1 A g^{-1} after 1000 cycles (Figure S10), which is higher than the TNO (76%) but lower than that of the DTNO@NC electrode (90%). This demonstrates the effect of the N-doped carbon encapsulation nanolayer, which is known to be able to stabilize the electrode-electrolyte interface during the repeated cycling processes.[38] Moreover, the DTNO@NC electrode still exhibits a significant EPR response signal at around g = 2.003 after 50 cycles at the current density of 1 A g^{-1} (Figure S11), this illustrates the existence of oxygen vacancies after cycling, together with further confirmed the internal reason of the DTNO@NC electrode with the favorable cycle stability.
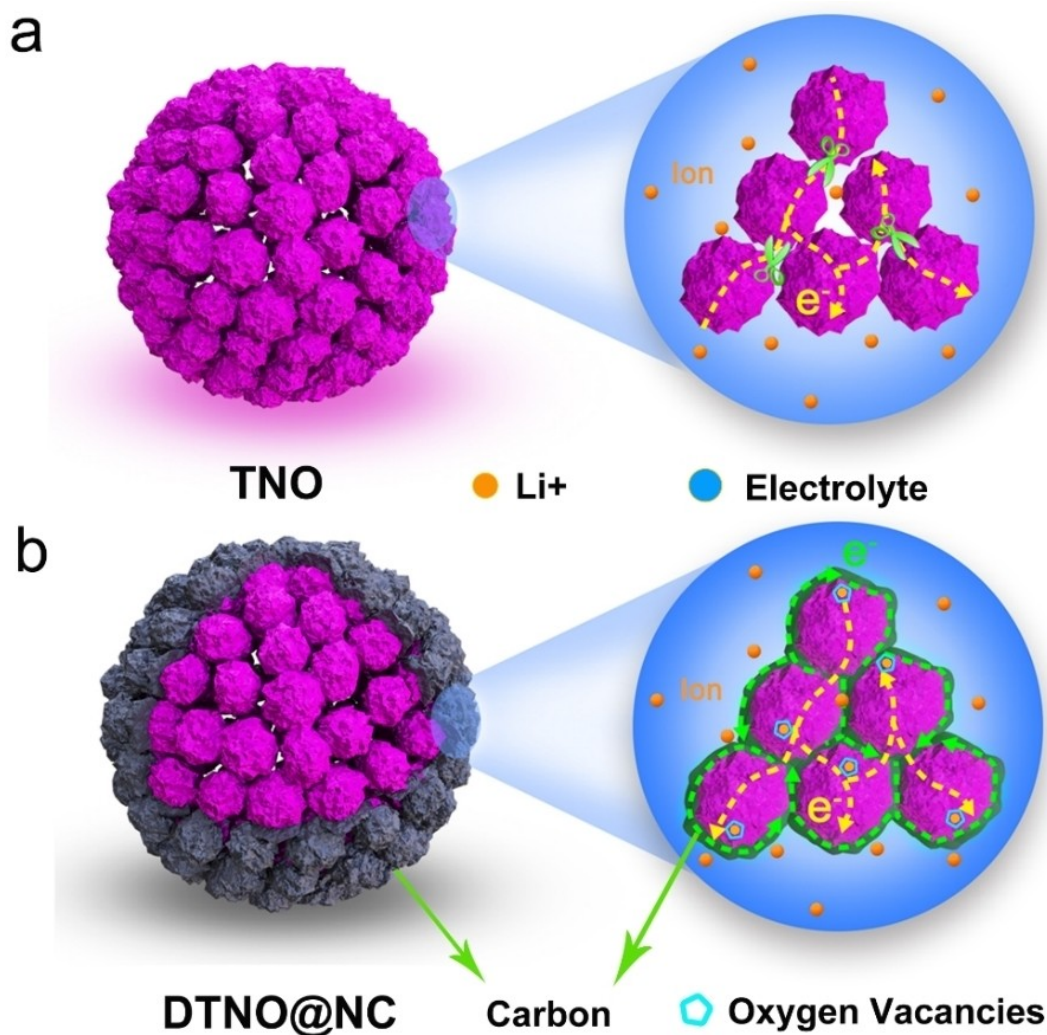
To further look at the advantages of the encapsulation of the oxygen-deficient TNO microspheres by the highly conductive N-doped carbon nanolayer in electrode, the lithium ion and electron transport diagrams of the TNO and DTNO@NC anodes are presented in Figure 5. As has been discussed, the TNO exhibits a microsphere morphology, composed of a large number of secondary nanoparticles, where there are gaps inevitably existing among these nanoparticles (Figure 5a). The boundary discontinuity will slow down the electron/charge transport among the secondary nanoparticles, where the energy barrier of Li$^+$ intercalation will be increased, as well as the intrinsic conductivity be decreased, and thus the overall performance of the bare TNO is not ideal. By the encapsulation, these secondary nanoparticles are covered with a rather uniform N-doped carbon nanolayer, which acts as a "bridge" to connect the gaps between the adjacent nanoparticles (Figure 5b), and thus electrons/charges will be transported quickly. Additionally, the N-doped carbon nanolayer prevents the direct contact between these nanoparticles and electrolyte, helping form a stable interface layer.[66] At the same time, the extra Li$^+$ can be stored in the formed oxygen deficiencies in crystals, and thus providing additional reaction sites and promoting the diffusion of Li ions.[43] Benefiting from both the oxygen-deficiency of TNO and N-doped carbon coating nanolayer, the DTNO@NC realizes higher conductivity, smaller charge resistance, more reactive active sites, and stable interface structure, resulting in superior rate capability and electrochemical performance. Notably, it is significant to compare the rate versus cycle performance of our fabricated DTNO@NC anode with other reported Ti–Nb oxides (**Table S2**). It found that the DTNO@NC anode is competitive to various anode materials, implying its more promising potential for practical application.

Galvanostatic intermittent titration technique (GITT) was employed to evaluate the Li$^+$ transport kinetics. As shown in Figure 6a and 6b, the transient voltage profiles of the TNO and DTNO@NC were characterized by GITT, where the galvanostatic discharge was for 5 min at a current density of 0.2 A g^{-1} and then rested for 20 min. The Li$^+$ diffusion coefficient (D_{Li^+}) can be calculated by Equation (1):[67]

$$D_{Li^+} = \frac{4}{\pi} \left(\frac{m_B V_M}{M_B S} \right)^2 \left(\frac{\Delta E_s}{\tau(dE_\tau/d\sqrt{\tau})} \right)^2 \left(\tau \ll \frac{L^2}{D_{Li^+}} \right) \quad (1)$$

where V_M, m_B, M_B, S and L represent the molar volume, the electrode active mass, the molar mass, the contact area between the electrode and electrolyte, and the average thickness of the electrode, respectively. Note that the applied current (i) is small, and the relaxation time (τ) is short, as well as the voltage and τ$^{1/2}$ of a single titration shows a good linear

Figure 5. Schematic diagram of lithium ion and electron transport mechanism for the a) TNO and b) DTNO@NC.

relationship for the TNO and DTNO@NC (Figure 6c and 6d), and thus Equation (1) can be simplified to Equation (2):

$$D_{Li^+} = \frac{4}{\pi\tau}\left(\frac{m_B V_M}{M_B S}\right)^2 \left(\frac{\Delta E_S}{\Delta E_\tau}\right)^2 \qquad (2)$$
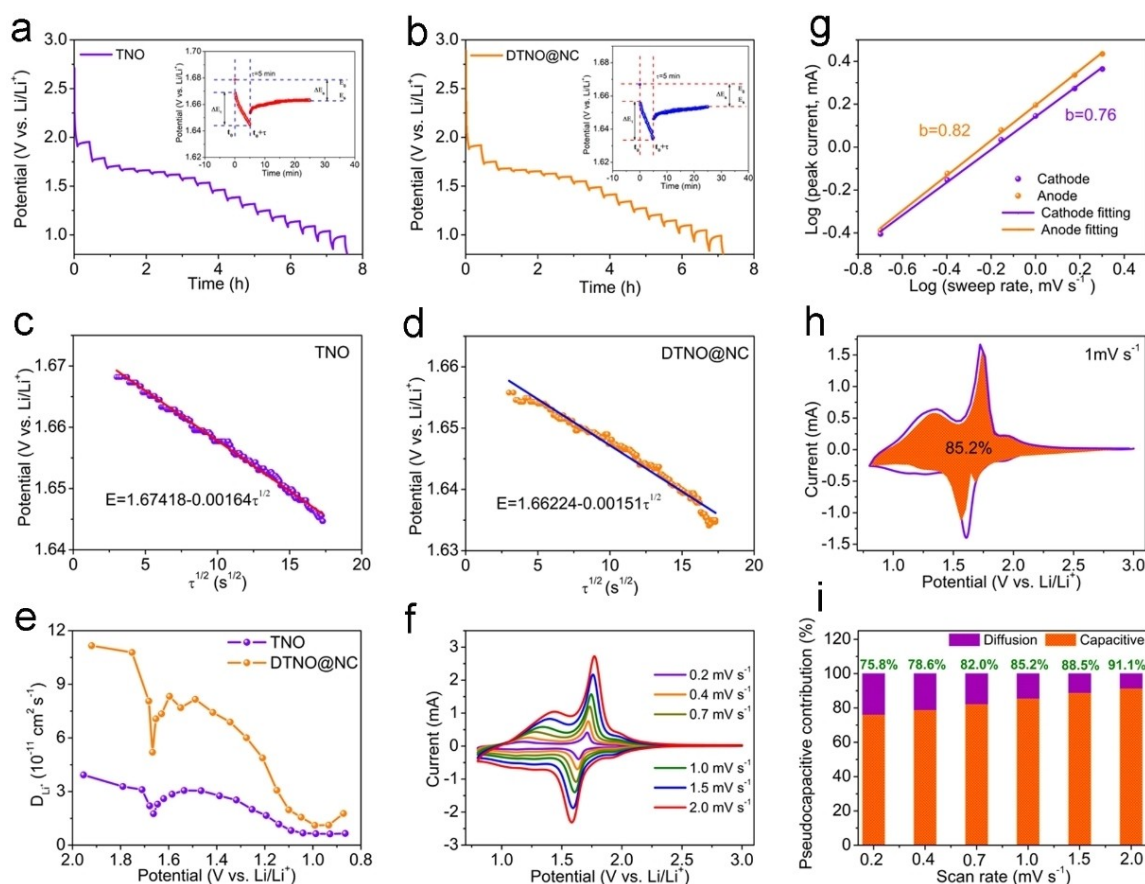
where ΔE_s represents the voltage change caused by the pulse, and ΔE_τ represents the voltage change of constant current charging (discharging) in the time range from t_0 to $t_{0+\tau}$ during the GITT process. In particular, the charge (discharge) voltage responses (ΔE_τ) are proportional to the *IR* drops, where the *R* represents the internal resistance of the battery system. Any changes between the redox reactions and voltages can affect the values of D_{Li}^+, but their overall trends are the same (Figure 6e), suggesting that the TNO and DTNO@NC have a similar Li$^+$-storage mechanism. Notably, the oxygen deficiency and N-doped carbon coating nanolayer can effectively increase the conductivity (including the electronic and ionic conductivity), and thus the charge (discharge) voltage responses (ΔE_τ) together with the *IR* drops can be effectively reduced, resulting in a higher D_{Li^+} for the DTNO@NC electrode, which is especially

obvious in the potential regions corresponding to the Nb$^{5+/4+}$ redox reaction. According to Fick's law ($\tau = L^2/2D$), the higher D_{Li}^+ of DTNO@NC electrode leads to a more rapid ion diffusion time, contributing to the excellent rate capability and cycle stability.

To understand in-depth the difference between the TNO and DTNO@NC, their electrochemical reaction kinetics and charge storage mechanism were investigated by CV measurements at different scan rates (0.2~2 mV s^{-1}). As shown in Figure 6f, there are a pair of prominent redox peaks of DTNO@NC in each cycle, which can well remain the peak shape and symmetry as the scan rate gradually increases, implying the excellent reversibility. While this pair of redox peaks of TNO has an obvious shift and deformation when the scan rates are increased (Figure S12a). Generally, the redox peak currents (*i*) and scan speeds (*v*) obey the power-law relationship, written as Equations (3) and (4):[68]

$$i = av^b \quad (3) \qquad\qquad (3)$$

$$\log(i) = b\log(v) + \log(a) \qquad\qquad (4)$$

Figure 6. a, b) Transient voltage profiles (inset of a single titration) by the GITT test, c, d) linear relationship between the potential and $\tau^{1/2}$ of a single titration, and e) calculated Li^+ diffusion coefficients for the TNO and DTNO@NC electrodes. f) CV curves at different scan rates, g) logarithm of peak currents *versus* the logarithm of scan rates, h) capacitive contribution at 1 mV s^{-1}, and i) capacitive contributions at various scan rates for the DTNO@NC electrode.

where i and v represent the redox peak current and scan speed, respectively. The a and b are variable. Notably, the value of b can be obtained by the slope of log (v) *versus* log (i). If $b=0.5$, it implies an ideal diffusion mechanism, and if $b=1$, it represents an ideal capacitive behavior. The logarithm of redox peak currents and scan rates (log (i) and log (v)) shows an obvious linear relationship. In particular, the cathodic and anodic peaks are corresponding to the b values with 0.50 and 0.53 of the TNO electrode (Figure S12b), suggesting the TNO electrode is almost controlled by a complete diffusion character. In comparison, the cathodic and anodic peaks are corresponding to the b values with 0.76 and 0.82 for the DTNO@NC electrode (Figure 6g), indicating that the DTNO@NC is controlled mainly by the pseudocapacitive behavior, and thus it shows a faster Li^+-storage capability.

To further quantify the pseudocapacitance contributions, the peak current response at a fixed voltage can be separated (diffusion-controlled and capacitive behaviors) by Equation (5):[68]

$$i = k_1 v + k_2 v^{1/2} \qquad (5)$$

where the k_1 and k_2 are constants. The response currents (i) can be quantified as $k_1 v$ (capacitive behavior) and $k_2 v^{1/2}$ (diffusion-

controlled behavior) at the corresponding potential (*V*), respectively. As shown in Figure 6h, the pseudocapacitance contribution of the DTNO@NC is about 85.2% at a scan rate of 1.0 mV s^{-1}, suggesting that the electrochemical kinetics are controlled mainly by capacitive behavior. It can be seen that the pseudocapacitance contributions increase continuously with the increase in the scan rates (Figure 6i). In particular, the pseudocapacitance contributions of DTNO@NC are 75.8, 78.6, 82.0, 85.2, 88.5 and 91.1% at 0.2, 0.4, 0.7, 1.0, 1.5 and 2.0 mV s^{-1}, respectively. Benefiting from the combined function of oxygen deficiency in TNO and N-doped carbon encapsulation nanolayer, DTNO@NC anode exhibits high pseudocapacitance characteristics, which facilitates a faster electrochemical reaction kinetic compared to the diffusion behavior, leading to an outstanding high rate ability and long-term cycling performance.

3. Conclusions

In summary, we have successfully synthesized DTNO@NC microspheres, with oxygen deficiency in $TiNb_{24}O_{62}$ and N-doped carbon encapsulating nanolayer, by a cost-effective aerosol spray process, followed by co-carbonization of the electroni-

cally coupled polydopamine layer in an argon atmosphere. The introduction of oxygen deficiencies improves the conductivity, reduces the Li^+ migration energy barrier, and increases active reaction sites. Besides, the N-doped carbon coating nanolayer not only further enhances the overall conductivity but also stabilizes the interface between the electrode and electrolyte. GITT and pseudocapacitance analysis demonstrate that the DTNO@NC exhibits a faster ion diffusion kinetics and significant pseudocapacitive behavior. Taken the synergistic effects of oxygen deficiency and N-doped carbon coating, the DTNO@NC shows much superior electrochemical performance than the pure TNO and other existing insertion anode materials. The new approach of effectively combining the intrinsic oxygen deficiency in $TiNb_{24}O_{62}$ and the extrinsic carbon encapsulation nanolayer demonstrated in the present work can be applied to other intercalation-type anode materials for electrochemical energy storage.

Experimental Section

Experimental details are found in the Supporting Information.

Conflict of Interest

The authors declare no conflict of interest.

[1] W. Zhang, D. H. Seo, T. Chen, L. Wu, M. Topsakal, Y. Zhu, D. Lu, G. Ceder, F. Wang, *Science* **2020**, *367*, 1030.
[2] H. Ji, J. Wu, Z. Cai, J. Liu, D. H. Kwon, H. Kim, A. Urban, J. K. Papp, E. Foley, Y. Tian, *Nat. Energy* **2020**, *5*, 213.
[3] X. Ji, *Energy Environ. Sci.* **2019**, *12*, 3203.
[4] J. W. Choi, D. Aurbach, *Nat. Rev. Mater.* **2016**, *1*, 1.
[5] M. Li, J. Lu, X. Ji, Y. Li, Y. Shao, Z. Chen, C. Zhong, K. Amine, *Nat. Rev. Mater.* **2020**, *1*, 1.
[6] J. Jiang, P. Nie, B. Ding, W. Wu, Z. Chang, Y. Wu, H. Dou, X. Zhang, *ACS Appl. Mater. Interfaces* **2016**, *8*, 30926.
[7] M. Liu, H. Fan, O. Zhuo, J. Chen, Q. Wu, L. Yang, L. Peng, X. Wang, R. Che, Z. Hu, *Nano Energy* **2020**, *68*, 104368.
[8] Q. Xia, Z. Lin, W. Lai, Y. Wang, C. Ma, Z. Yan, Q. Gu, W. Wei, J. Z. Wang, Z. Zhang, *Angew. Chem. Int. Ed.* **2019**, *58*, 14125.
[9] Y. Li, H. Wang, L. Wang, Z. Mao, R. Wang, B. He, Y. Gong, X. Hu, *Small* **2019**, *15*, 1804539.
[10] Y. Li, R. Zhang, W. Zhou, X. Wu, H. Zhang, J. Zhang, *ACS Nano* **2019**, *13*, 5533.
[11] L. Wu, J. Zheng, L. Wang, X. Xiong, Y. Shao, G. Wang, J. H. Wang, S. Zhong, M. Wu, *Angew. Chem. Int. Ed.* **2019**, *131*, 821.
[12] L. Hu, Y. Ren, H. Yang, Q. Xu, *ACS Appl. Mater. Interfaces* **2014**, *6*, 14644.
[13] L. C. Loaiza, L. Monconduit, V. Seznec, *Small* **2020**, 1905260.
[14] J. Shin, T. H. Kim, Y. Lee, E. Cho, *Energy Storage Mater.* **2019**, *25*, 764.
[15] P. Nie, X. Liu, R. Fu, Y. Wu, J. Jiang, H. Dou, X. Zhang, *ACS Energy Lett.* **2017**, *2*, 1279.
[16] J. T. Han, Y. H. Huang, J. B. Goodenough, *Chem. Mater.* **2011**, *23*, 2027.
[17] K. Tang, X. Mu, P. A. van Aken, Y. Yu, J. Maier, *Adv. Energy Mater.* **2013**, *3*, 49.
[18] H. Park, H. B. Wu, T. Song, X. W. Lou, U. Paik, *Adv. Energy Mater.* **2015**, *5*, 1401945.
[19] H. Park, T. Song, U. Paik, *J. Mater. Chem. A* **2015**, *3*, 8590.
[20] H. Yu, H. Lan, L. Yan, S. Qian, X. Cheng, H. Zhu, N. Long, M. Shui, J. Shu, *Nano Energy* **2017**, *38*, 109.
[21] S. Lou, X. Cheng, Y. Zhao, A. Lushington, J. Gao, Q. Li, P. Zuo, B. Wang, Y. Gao, Y. Ma, *Nano Energy* **2017**, *34*, 15.
[22] L. Yin, D. Pham Cong, I. Jeon, J. P. Kim, J. Cho, S. Y. Jeong, H. W. Lee, C. R. Cho, *Chem. Eng. J.* **2020**, *382*, 122800.
[23] Y. Yuan, H. Yu, X. Cheng, R. Zheng, T. Liu, N. Peng, N. Long, M. Shui, J. Shu, *Chem. Eng. J.* **2019**, *374*, 937.
[24] C. Lin, G. Wang, S. Lin, J. Li, L. Lu, *Chem. Commun.* **2015**, *51*, 8970.
[25] R. Sun, G. Liu, S. Cao, B. Dong, X. Liu, M. Hu, M. Liu, X. Duan, *Dalton Trans.* **2017**, *46*, 17061.
[26] X. Liu, G. Liu, M. Liu, M. Hu, Y. Hu, J. Ma, *J. Alloys Compd.* **2019**, *787*, 344.
[27] S. Deng, D. Chao, Y. Zhong, Y. Zeng, Z. Yao, J. Zhan, Y. Wang, X. Wang, X. Lu, X. Xia, *Energy Storage Mater.* **2018**, *12*, 137.
[28] S. Lou, X. Cheng, J. Gao, Q. Li, L. Wang, Y. Cao, Y. Ma, P. Zuo, Y. Gao, C. Du, *Energy Storage Mater.* **2018**, *11*, 57.
[29] Z. Yao, X. Xia, Y. Zhang, D. Xie, C. Ai, S. Lin, Y. Wang, S. Deng, S. Shen, X. Wang, *Nano Energy* **2018**, *54*, 304.
[30] X. Xia, S. Deng, S. Feng, J. Wu, J. Tu, *J. Mater. Chem. A* **2017**, *5*, 21134.
[31] W. L. Wang, B. Y. Oh, J. Y. Park, H. Ki, J. Jang, G. Y. Lee, H. B. Gu, M. H. Ham, *J. Power Sources* **2015**, *300*, 272.
[32] C. Lin, S. Deng, D. J. Kautz, Z. Xu, T. Liu, J. Li, N. Wang, F. Lin, *Small* **2017**, *13*, 1702903.
[33] C. Yang, S. Deng, C. Lin, S. Lin, Y. Chen, J. Li, H. Wu, *Nanoscale* **2016**, *8*, 18792.
[34] K. J. Griffith, A. Senyshyn, C. P. Grey, *Inorg. Chem.* **2017**, *56*, 4002.
[35] A. Wadsley, *Acta Crystallogr.* **1961**, *14*, 660.
[36] S. Li, J. Chen, X. Gong, J. Wang, P. S. Lee, *NPG Asia Mater.* **2018**, *10*, 406.
[37] H. Yu, X. Cheng, H. Zhu, R. Zheng, T. Liu, J. Zhang, M. Shui, Y. Xie, J. Shu, *Nano Energy* **2018**, *54*, 227.
[38] Y. Zhang, Z. Ding, C. W. Foster, C. E. Banks, X. Qiu, X. Ji, *Adv. Funct. Mater.* **2017**, *27*, 1700856.
[39] M. Han, J. Huang, S. Liang, L. Shan, X. Xie, Z. Yi, Y. Wang, S. Guo, J. Zhou, *iScience* **2020**, *23*, 100797.
[40] H. E. Wang, K. Yin, N. Qin, X. Zhao, F.-J. Xia, Z. Y. Hu, G. Guo, G. Cao, W. Zhang, *J. Mater. Chem. A* **2019**, *7*, 10346.
[41] G. Fang, C. Zhu, M. Chen, J. Zhou, B. Tang, X. Cao, X. Zheng, A. Pan, S. Liang, *Adv. Funct. Mater.* **2019**, *29*, 1808375.
[42] Y. Zhang, L. Tao, C. Xie, D. Wang, Y. Zou, R. Chen, Y. Wang, C. Jia, S. Wang, *Adv. Mater.* **2020**, *32*, 1905923.
[43] Y. Wang, X. Xiao, Q. Li, H. Pang, *Small* **2018**, *14*, 1802193.
[44] S. Deng, H. Zhu, G. Wang, M. Luo, S. Shen, C. Ai, L. Yang, S. Lin, Q. Zhang, L. Gu, *Nat. Commun.* **2020**, *11*, 1.
[45] M. Hu, W. Yang, H. Tan, L. Jin, L. Zhang, P. Kerns, Y. Dang, S. Dissanayake, B. Schaefer, B. Liu, *Matter* **2020**, *2*, 1244.
[46] T. Lin, C. Yang, Z. Wang, H. Yin, X. Lü, F. Huang, J. Lin, X. Xie, M. Jiang, *Energy Environ. Sci.* **2014**, *7*, 967.
[47] X. Chen, L. Liu, Y. Y. Peter, S. S. Mao, *Science* **2011**, *331*, 746.
[48] G. Wang, Y. Yang, Y. Ling, H. Wang, X. Lu, Y. C. Pu, J. Z. Zhang, Y. Tong, Y. Li, *J. Mater. Chem. A* **2016**, *4*, 2849.
[49] Q. Gan, H. He, K. Zhao, Z. He, S. Liu, S. Yang, *ACS Appl. Mater. Interfaces* **2018**, *10*, 7031.

[50] P. Nie, G. Xu, J. Jiang, H. Dou, Y. Wu, Y. Zhang, J. Wang, M. Shi, R. Fu, X. Zhang, *Small Methods* **2018**, *2*, 1700272.

[51] J. S. Park, J. K. Kim, J. H. Hong, J. S. Cho, S.-K. Park, Y. C. Kang, *Nanoscale* **2019**, *11*, 19012.

[52] P. Nie, Z. Le, G. Chen, D. Liu, X. Liu, H. B. Wu, P. Xu, X. Li, F. Liu, L. Chang, *Small* **2018**, *14*, 1800635.

[53] J. Wu, G. Pan, W. Zhong, L. Yang, S. Deng, X. Xia, *J. Colloid Interface Sci.* **2020**, *562*, 511.

[54] Z. Li, Y. Dong, J. Feng, T. Xu, H. Ren, C. Gao, Y. Li, M. Cheng, W. Wu, M. Wu, *ACS Nano* **2019**, *13*, 9227.

[55] T. Ding, Y. Xing, Z. Wang, H. Guan, L. Wang, J. Zhang, K. Cai, *Nanoscale Horiz.* **2019**, *4*, 652.

[56] S. Deng, Y. Zhang, D. Xie, L. Yang, G. Wang, X. Zheng, J. Zhu, X. Wang, Y. Yu, G. Pan, *Nano Energy* **2019**, *58*, 355.

[57] Z. Yao, X. Xia, S. Zhang, C. Zhou, G. Pan, Q. Xiong, Y. Wang, X. Wang, J. Tu, *Energy Storage Mater.* **2020**, *25*, 555.

[58] J. Jiang, J. Yuan, P. Nie, Q. Zhu, C. Chen, W. He, T. Zhang, H. Dou, X. Zhang, *J. Mater. Chem. A* **2020**, *8*, 3956.

[59] J. Jiang, P. Nie, B. Ding, Y. Zhang, G. Xu, L. Wu, H. Dou, X. Zhang, *J. Mater. Chem. A* **2017**, *5*, 23283.

[60] L. Yan, J. Shu, C. Li, X. Cheng, H. Zhu, H. Yu, C. Zhang, Y. Zheng, Y. Xie, Z. Guo, *Energy Storage Mater.* **2019**, *16*, 535.

[61] C. Lin, L. Hu, C. Cheng, K. Sun, X. Guo, Q. Shao, J. Li, N. Wang, Z. Guo, *Electrochim. Acta* **2018**, *260*, 65.

[62] Q. Fu, J. Hou, R. Lu, C. Lin, Y. Ma, J. Li, Y. Chen, *Mater. Lett.* **2018**, *214*, 60.

[63] C. Yang, S. Yu, C. Lin, F. Lv, S. Wu, Y. Yang, W. Wang, Z. Z. Zhu, J. Li, N. Wang, *ACS Nano* **2017**, *11*, 4217.

[64] Y. Zhang, M. Zhang, Y. Liu, H. Zhu, L. Wang, Y. Liu, M. Xue, B. Li, X. Tao, *Electrochim. Acta* **2020**, *330*, 135299.

[65] F. Lu, Q. Chen, S. Geng, M. Allix, H. Wu, Q. Huang, X. Kuang, *J. Mater. Chem. A* **2018**, *6*, 24232.

[66] B. Liu, S. Sun, R. Jia, H. Zhang, X. Zhu, C. Zhang, J. Xu, T. Zhai, H. Xia, *Adv. Funct. Mater.* **2020**, *30*, 1909546.

[67] J. Jiang, Y. Zhang, Y. An, L. Wu, Q. Zhu, H. Dou, X. Zhang, *Small Methods* **2019**, *3*, 1900081.

[68] V. Augustyn, J. Come, M. A. Lowe, J. W. Kim, P. L. Taberna, S. H. Tolbert, H. D. Abruña, P. Simon, B. Dunn, *Nat. Mater.* **2013**, *12*, 518.